

# FADPNet: Frequency-Aware Dual-Path Network for Face Super-Resolution

Siyu Xu, Wenjie Li, Guangwei Gao, *Senior Member, IEEE*, Jian Yang, *Member, IEEE*,  
Guo-Jun Qi, *Fellow, IEEE*, and Chia-Wen Lin, *Fellow, IEEE*

**Abstract**—Face super-resolution (FSR) under limited computational costs remains an open problem. Existing approaches typically treat all facial pixels equally, resulting in suboptimal allocation of computational resources and degraded FSR performance. CNN is relatively sensitive to high-frequency facial features, such as component contours and facial outlines. Meanwhile, Mamba excels at capturing low-frequency features like facial color and fine-grained texture, and does so with lower complexity than Transformers. Motivated by these observations, we propose FADPNet, a Frequency-Aware Dual-Path Network that decomposes facial features into low- and high-frequency components and processes them via dedicated branches. For low-frequency regions, we introduce a Mamba-based Low-Frequency Enhancement Block (LFEB), which combines state-space attention with squeeze-and-excitation operations to extract low-frequency global interactions and emphasize informative channels. For high-frequency regions, we design a CNN-based Deep Position-Aware Attention (DPA) module to enhance spatially-dependent structural details, complemented by a lightweight High-Frequency Refinement (HFR) module that further refines frequency-specific representations. Through the above designs, our method achieves an excellent balance between FSR quality and model efficiency, outperforming existing approaches.

**Index Terms**—Face super-resolution, Mamba, Frequency feature, Dual-Path, Efficiency.

## I. INTRODUCTION

FACE super-resolution (FSR), also known as face hallucination, focuses on reconstructing high-resolution (HR) facial images from low-resolution (LR) inputs. FSR plays a critical role in real-world scenarios where LR faces may appear in surveillance videos, historical archives, or mobile imaging. Enhancing facial image resolution is essential for improving downstream tasks such as face recognition [1], face alignment [2], and facial attribute analysis [3].

Siyu Xu and Guangwei Gao are with the Institute of Advanced Technology, Nanjing University of Posts and Telecommunications, Nanjing 210046, China, Key Laboratory of Artificial Intelligence, Ministry of Education, Shanghai 200240, and also with the Provincial Key Laboratory for Computer Information Processing Technology, Soochow University, Suzhou 215006, China (e-mail: csggao@gmail.com, xusiyu200107@163.com).

Wenjie Li is with the School of Artificial Intelligence, Beijing University of Posts and Telecommunications, Beijing 100080, China (e-mail: lewj2408@gmail.com).

Jian Yang is with the School of Computer Science and Technology, Nanjing University of Science and Technology, Nanjing 210094, China (e-mail: csjyang@njjust.edu.cn).

Guo-Jun Qi is with the Research Center for Industries of the Future and the School of Engineering, Westlake University, Hangzhou 310024, China, and also with OPPO Research, Seattle, WA 98101 USA (e-mail: guojunq@gmail.com).

Chia-Wen Lin is with the Department of Electrical Engineering and the Institute of Communications Engineering, National Tsing Hua University, Hsinchu 300044, Taiwan 30013, R.O.C. (e-mail: cwlin@ee.nthu.edu.tw).

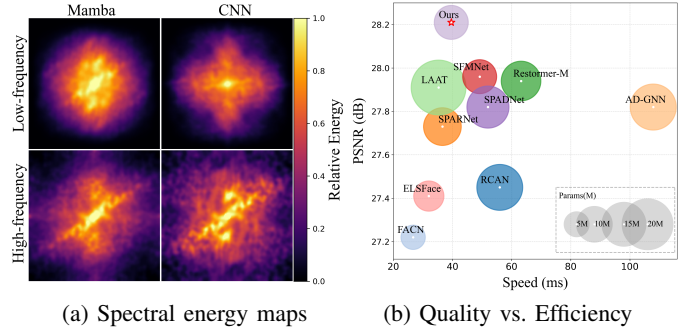


Fig. 1: (a) Spectral energy distribution of features extracted by Mamba and CNN architectures, where Mamba exhibits concentrated low-frequency responses compared to CNN’s high-frequency sensitivity. Color intensity corresponds to normalized energy values. (b) Efficiency trade-offs on CelebA test set [4], demonstrating our method’s optimal balance between PSNR, Params, and inference speed.

One fundamental challenge in FSR lies in the long-tailed distribution of image frequency components [5]. High-frequency parts, such as the eyes, nose, mouth, and facial contours, account for a small portion of the facial area but require disproportionate modeling capacity due to their high variability. These regions are particularly sensitive to identity, illumination, and expression changes, making them significantly harder [6] to reconstruct than low-frequency areas such as skin, which contribute little to identity-specific features. This imbalance results in a performance bottleneck, where failure to recover high-frequency content leads to perceptual degradation. However, most existing methods treat all pixels equally, ignoring the skewed distribution of visual complexity and importance. This uniform processing strategy leads to inefficient resource usage and suboptimal reconstruction quality. While some methods attempt to separate frequency components [7], [8], they often struggle to maintain a balanced representation across global and local facial structures.

To address these limitations, we aim to adaptively distinguish and process high- and low-frequency information. Meanwhile, we wonder about a dual-path feature fusion to help resolve the imbalance between local and global modeling that arises in previous frequency-aware methods, ultimately enabling more efficient and accurate FSR. As shown in Fig. 1a, we present the spectral energy maps generated by CNN [9], and Mamba [10]. Interestingly, Mamba exhibits broader responses in the low-frequency regions of facial images, whereas CNN tends to be more sensitive to high-frequency

components. Moreover, compared to the Transformer [11] framework, Mamba achieves global modeling through scanning mechanisms, thus keeping the computational complexity within a linear range and avoiding the expensive quadratic cost. These observations lead us to consider an alternative design: could we develop a two-branch architecture that allows Mamba and CNN to each specialize in the frequency domains they are most suited for, while integrating their outputs to better balance global and local facial structure representation?

Based on the above observations and analysis, we propose a Frequency-Aware Dual-Path Network (FADPNet), which allocates distinct submodules to specialize in different frequency domains. In particular, we introduce the Low-Frequency Enhancement Block (LFEB) and High-Frequency Enhancement Block (HFEB) to extract and refine, respectively, stable identity-preserving low-frequency features and fine-grained, structure-critical high-frequency details. The LFEB integrates an Attentive State Space Block (ASSB) and a Squeeze-and-Excitation Block (SEB) to enhance low-frequency features. At the same time, the HFEB combines a High-Frequency Refinement (HFR) module and a Depthwise Position-aware Attention (DPA) module to refine high-frequency details. These two modules integrate complementary modeling strategies—global and local—to better capture the intrinsic characteristics of facial components across different frequency levels. By decomposing and processing features based on their frequency significance, our approach not only enhances facial fidelity but also improves computational efficiency by focusing resources on perceptually important regions. As shown in Fig. 1b, our proposed FADPNet achieves superior efficiency and reconstruction quality compared to existing FSR methods. In summary, the main contributions are as follows:

- We propose the LFEB, which combines ASSB and SEB to enhance facial low-frequency representations by capturing global structures and emphasizing informative channel-wise responses.
- We propose the HFEB, which combines HFR and DPA to strengthen local high-frequency facial structures and further capture long-range spatial dependencies to adaptively refine high-frequency contexts.
- Based on the architecture designed from our frequency analysis, our FADPNet demonstrates competitive FSR ability relative to existing FSR methods across performance, model size, and inference speed.

## II. RELATED WORK

### A. Face Super-Resolution

Face super-resolution [12] has made notable strides with the advancement of deep learning. Early approaches [8], [13]–[15] leverage explicit facial priors to guide reconstruction. For instance, FSRNet [13] incorporated facial landmarks and parsing maps to enforce structural consistency, while FAN [8] applied a face alignment network with progressive training to enhance realism. DIC [14] introduced an iterative refinement loop combining facial components and landmark predictions. To improve the representation of facial spatial features, Hu *et*

*al.* [15] first utilized 3D shape priors in the network to better preserve sharp facial spatial structures.

However, prior-based methods depend heavily on accurate prior estimation, which is unreliable at extremely LR scenes and adds computational overhead. To mitigate this, recent works have adopted attention-based [16] or data-driven strategies [17]. SPARNet [16] used spatial attention to focus on key facial regions. SISN [18] decoupled attention into structural and textural streams. AD-GNN [19] combined spatial attention with graph-based message passing to model feature dependencies. LAAT [20] introduced local-aware refinement within a Transformer framework to enhance detail, while SCTANet [21] jointly modeled spatial and channel attention. SFMNet [22] employed parallel frequency-spatial branches for multi-scale feature learning. WFEN [23] used wavelet-based encoding to mitigate downsampling artifacts. *However, existing FSR methods apply uniform processing across spatial regions, overlooking the varying complexity of frequency components. In contrast, our method introduces a frequency-aware dual-path design that adaptively handles high- and low-frequency features at multiple scales, leading to more robust and detail-preserving reconstruction under LR conditions.*

### B. Long-Range Modeling

Modeling long-range dependencies is vital for FSR, as facial structures span distant spatial regions. Transformer-based methods [20], [22], [24] have demonstrated strong global modeling via self-attention. For example, LAAT [20] enhanced fine-grained facial modeling via self-refinement in a Transformer framework, improving detail restoration. SFMNet [22] adopted spatial and frequency branches to jointly capture global and local features across diverse receptive fields. CTCNet [25] further enhanced FSR by fusing multi-scale global representations extracted from Transformers.

However, vision Transformers [25]–[27] suffer from quadratic complexity, limiting their scalability. This challenge has prompted exploration of alternative long-range modeling with lower computational cost. Structured State-Space Models (SSMs) [28] have gained attention for their linear-time global modeling capability. Notably, Mamba [10] introduced a selective scan mechanism for efficient long-sequence processing while preserving strong global context, and has been successfully adapted to visual tasks [29], [30]. Building on this, MambaIR [31] extended Mamba to image restoration, alleviating issues such as local pixel forgetting and redundant channel representations. Variants like MambaLLIE [32] further demonstrate its adaptability to various low-level vision tasks.

Despite its efficiency, Mamba inherits a causal bias from its sequence-oriented design, which conflicts with the non-causal nature of super-resolution [31] and limits spatial modeling. To address this, MambaIRv2 [33] introduced direction-agnostic scanning for richer context modeling with linear scalability. *Unlike existing Mamba-based methods [31]–[33], our approach incorporates a customized non-causal state-space backbone into the low-frequency branch, explicitly designed for face super-resolution to better preserve structural consistency and global facial context.*

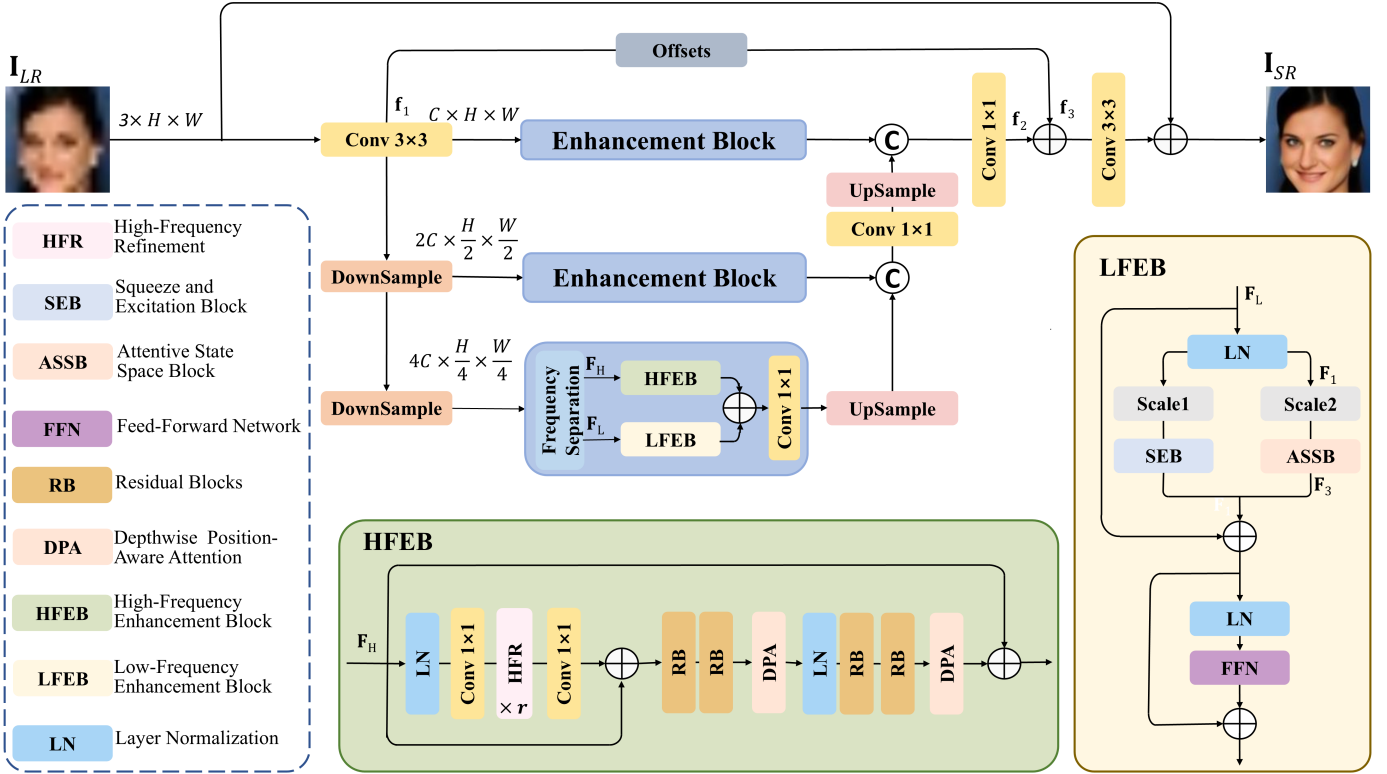


Fig. 2: Overview of our FADPNet, which adopts a U-Shape structure composed of HFEBs for high-frequency facial feature modeling and LFEBs for low-frequency facial feature enhancement.

### C. Frequency-Aware Super-Resolution

Frequency-aware SR methods have emerged as an effective paradigm for enhancing structure, particularly in edges and textures [34]–[36]. By decomposing image content into distinct frequency bands, these methods enable neural networks to more precisely model the unique characteristics of each frequency component [37]. This design aligns with the well-established observation that low-frequency components mainly represent smooth and homogeneous regions, whereas high-frequency components capture fine-grained details and edge features essential for perceptual quality [38].

Explicit transformation methods decompose the image reconstruction process into frequency-specific operations. For instance, wavelet-based methods like SRCliqueNet [38] applied a discrete wavelet transform to separate LR images into sub-bands, which are then processed by specialized subnetworks to sharpen high-frequency components while preserving low-frequency structures. Similarly, FreqNet [35] operated in the discrete cosine transform domain, predicting HR frequency coefficients through learnable spectral decoders. In contrast, implicit methods achieve frequency awareness through architectural design. SRDN [39] used high-pass constrained convolutions and residual connections to emphasize high-frequency propagation, while FSN [34] adopted Octave Convolution to split features into frequency-aware streams. AFD [40] estimated feature drifting in the DCT frequency domain, adaptively enhances features. However, the above methods either concentrate solely on high-frequency enhancement [41] or fail to model the interaction between global low-frequency

structures and local high-frequency details. To address this, we propose a dual-branch framework that separately models frequency-specific features, improving both reconstruction quality and computational efficiency.

## III. PROPOSED METHOD

### A. Overview of FADPNet

The proposed network architecture, as illustrated in Fig. 2, implements a hierarchical frequency-aware processing framework. It commences with an input image  $\mathbf{I}_{LR} \in \mathbb{R}^{3 \times H \times W}$  from which shallow facial features  $\mathbf{f}_1 \in \mathbb{R}^{C \times H \times W}$  are extracted. Our architecture adopts a three-level U-Net [42] structure, where each resolution stage includes a cascaded basic block that decomposes features into high- and low-frequency components for separate processing. The High-Frequency Enhancement Block (HFEB) restores fine-grained details using convolutions, Residual Blocks (RB), a High-Frequency Refinement (HFR) module, and a Depthwise Position-Aware Attention (DPA) module. The Low-Frequency Enhancement Block (LFEB) employs a dual-branch design: the Squeeze-and-Excitation Block (SEB) enhances local identity cues, while the Attentive State Space Block (ASSB) captures global facial structure. Outputs are fused and refined through a Feed-Forward Network (FFN). To reduce spatial misalignment caused by downsampling and upsampling, we introduce an offset-based warping module that aligns coarse structures with fine-level details, improving cross-scale consistency. Finally, features from all levels are fused and dimensionality reduction to reconstruct an HR face image  $\mathbf{I}_{SR} \in \mathbb{R}^{3 \times H \times W}$ .

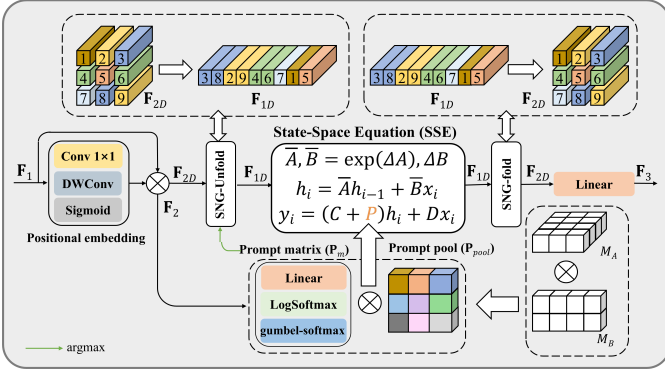


Fig. 3: The architecture of Attentive State Space Block (ASSB)

### B. Low-Frequency Enhancement Block (LFEB)

Our Low-Frequency Enhancement Block (LFEB) is designed to model low-frequency facial features, such as smooth skin regions on the forehead, cheeks, and chin, which exhibit gradual intensity variations and contain minimal identity-specific details. Specifically, given a low-frequency feature  $F_L \in \mathbb{R}^{C \times H \times W}$  extracted from the frequency separation module. First, LFEB begins with a layer normalization for stable training, followed by a dual-branch structure: the Squeeze-and-Excitation Block (SEB) [43] for adaptively calibrating feature channels to improve the focus on important features, while the Attentive State Space Block (ASSB) captures global facial structure. A learnable fusion scheme adaptively balances two feature streams, guided by scaling parameters optimized during training. The fused output is further processed by a Feed-Forward Network (FFN) [10] and combined with the block’s input via a residual connection. This design enhances identity-salient, low-frequency attributes such as coarse facial shape and alignment while preserving photorealistic appearance.

1) *Attentive State Space Block (ASSB)*: As shown in Fig. 3, building upon the Mamba [11] framework, ASSB introduces non-causal global modeling through an integration of semantic perceptual sequence reorganization and a cue-guided attention mechanism, which is used to address the limitations of causal modeling in the traditional state-space. Specifically, it begins by applying a positional embedding to the input feature  $F_1 \in \mathbb{R}^{C \times H \times W}$  to obtain a feature  $F_2 \in \mathbb{R}^{C \times H \times W}$ :

$$F_2 = F_1 \cdot \sigma(\text{DWConv}_{3 \times 3}(\text{Conv}_1(F_1))), \quad (1)$$

where  $\text{Conv}_1$  is a  $1 \times 1$  convolution,  $\text{DWConv}_{3 \times 3}$  denotes a  $3 \times 3$  depthwise convolution and  $\sigma(\cdot)$  denotes sigmoid activation. After that, to transcend the causal constraints of standard Mamba architectures, we incorporate the learned prompts  $P$  into a conventional State-Space Equation (SSE), enabling richer spatial interactions beyond sequential dependency. The final prompt representation  $P$  consists of two components: a prompt pool  $P_{pool}$  and a prompt matrix  $P_m$ :

$$P = P_m \cdot P_{pool}. \quad (2)$$

The prompt pool is parameterized via low-rank decomposition for efficiency. The shared basis  $M_A$  captures cross-

block semantic commonality, while block-specific  $M_B$  enables adaptive feature combination:

$$P_{pool} = M_A \cdot M_B, \quad (3)$$

$$M_A \in \mathbb{R}^{T \times r}, M_B \in \mathbb{R}^{r \times d} \quad (r \ll \min\{T, d\}), \quad (4)$$

where  $r$  is the inner rank,  $T$  is the number of prompts and  $d$  is the number of hidden states in Mamba. Instance-specific prompt matrix is governed by a routing mechanism employing gumbel-softmax [44], which generates  $L$  instance-specific prompts  $P_m \in \mathbb{R}^{L \times T}$  dynamically associated input pixels with relevant prompts from the pool:

$$P_m = \text{gumbel-softmax}(\text{LogSoftmax}(W_p \cdot F_2)), \quad (5)$$

where  $W_p$  denotes the linear layer,  $\text{LogSoftmax}$  refers to the logarithm of the softmax function, and  $\text{gumbel-softmax}$  is a gumbel softmax [44] operator. Then, the Semantic Guided Neighboring (SGN) unfolds this 2D feature  $F_2$  into 1D sequences for SSE. SGN-Unfold mechanism redefines the traditional spatial-to-sequential transformation by dynamically reorganizing pixels into 1D sequences based on semantic similarity, effectively mitigating the long-range decay inherent to existing models [33]. Notably, the semantic information that the mechanism relies on during this process stems from the prompt matrix  $P_m$ :

$$\text{Index} = \text{argmax}(P_m, \text{dim} = -1). \quad (6)$$

$$F_{1D} = \text{SNG}(F_{2D}, \text{Index}). \quad (7)$$

Tokens are subsequently sorted based on their semantic indices to group semantically similar tokens into contiguous sequences. Central to ASSB operation is SSE, a modified state-space formulation that transcends the causal constraints of standard Mamba architectures. SSE enhances the output matrix  $C$  by incorporating learnable semantic prompts—compact embeddings representing pixel groups with shared semantics. This formulation injects global contextual awareness into SSE:

$$y_i = (C + P)h_i + Dx_i \quad (8)$$

Finally, an SGN-fold is applied as the inverse operation, reconstructing the semantically sorted sequence back into the original spatial layout to form the 2D feature. This reversal is guided by the previously computed reverse index, ensuring accurate spatial alignment. The restored feature is then passed through a linear projection to produce the final output feature  $F_3$ . Critically, this architecture enables single-directional scanning—unlike conventional bidirectional Mamba variants requiring multiple scans—reducing computational redundancy while preserving global coherence. This efficiency breakthrough not only accelerates inference but also facilitates seamless integration with subsequent enhancement stages, where the refined low-frequency features serve as stable anchors for high-frequency detail reconstruction.

### C. High-Frequency Enhancement Block (HFEB)

In our method, HFEB specializes in high-frequency detail recovery. Specifically, for the high-frequency feature

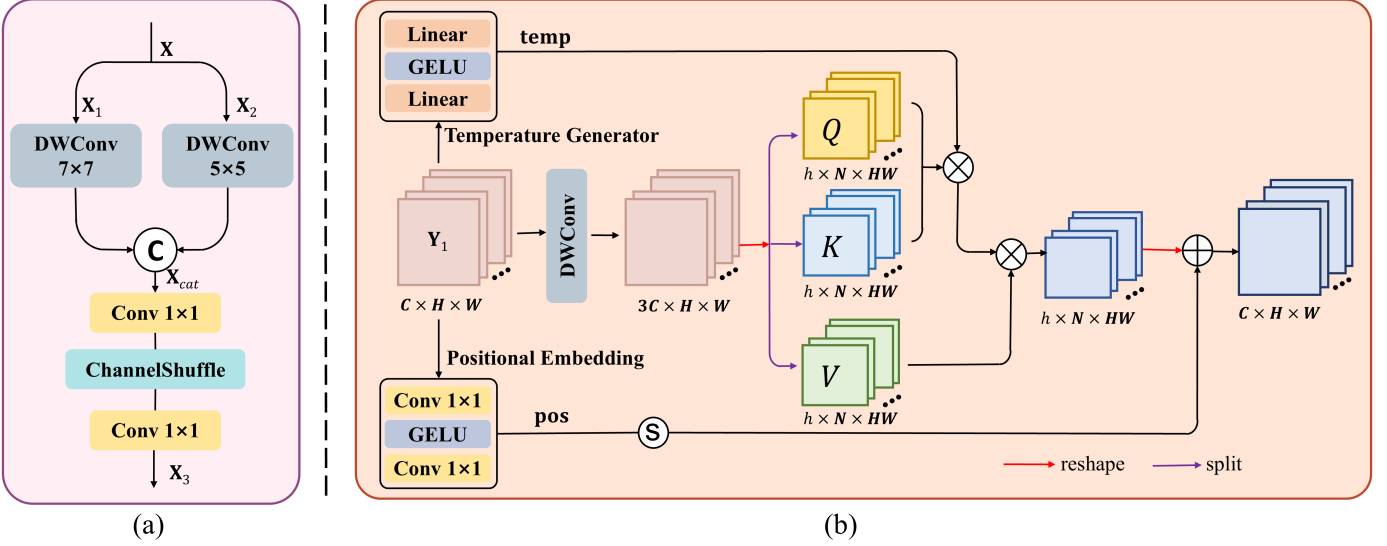


Fig. 4: The architecture of (a) High-Frequency Refinement (HFR) (b) Depthwise Position-aware Attention (DPA)

$\mathbf{F}_H \in \mathbb{R}^{C \times H \times W}$  obtained from frequency separation operator, we first apply a  $1 \times 1$  convolution to reduce channels to  $\frac{C}{2}$  to minimize computational costs. Then we use a  $1 \times 1$  convolution to expand channels to  $C$  for follow-up operation. Subsequently, from a local enhancement perspective, features traverse a sequence of our High-Frequency Refinement (HFR), which progressively extracts hierarchical high-frequency patterns, strengthening details through iterative feature transformation. From a global modeling angle, interspersed among subsequent residual blocks, Depthwise Position-aware Attention (DPA) modules selectively enhance critical high-frequency facial attributes, while preserving facial realism through adaptive feature modulation. This synergistic operation establishes essential groundwork for achieving high-fidelity face super-resolution.

1) *High-Frequency Refinement (HFR)*: As shown in Fig. 4 (a), our HFR module operates in a recurrent manner, to iteratively refine high-frequency components—fine-grained facial details like eyes, eyebrows, and lips—over  $r$  cycles. Given an input feature  $\mathbf{X} \in \mathbb{R}^{C \times H \times W}$ , the module first extracts multi-scale spatial features through parallel depth-wise separable convolutions with complementary receptive fields:

$$\mathbf{X}_1 = \text{DWConv}_{7 \times 7}(\mathbf{X}), \quad \mathbf{X}_2 = \text{DWConv}_{5 \times 5}(\mathbf{X}), \quad (9)$$

where the  $7 \times 7$  kernel captures broad contextual patterns (e.g., structural contours) and the  $5 \times 5$  kernel focuses on localized details (e.g., fine textures). These multi-scale outputs are concatenated along the channel dimension to obtain  $\mathbf{X}_{cat}$ :

$$\mathbf{X}_{cat} = \text{Concat}[\mathbf{X}_1, \mathbf{X}_2]. \quad (10)$$

To integrate hierarchical spatial information. Then a  $1 \times 1$  convolution compresses the concatenated features into the original channel dimension while learning cross-scale correlations. To mitigate channel grouping-induced information isolation, a channel shuffle operation and a second  $1 \times 1$  convolution are applied to get  $\mathbf{X}_3$ :

$$\mathbf{X}_3 = \text{Conv}_4 \cdot \text{CS}(\text{Conv}_3 \cdot \mathbf{X}_{cat}), \quad (11)$$

where  $\text{Conv}_3$  is a  $1 \times 1$  convolution for channel expansion,  $\text{CS}(\cdot)$  denotes channel-shuffle and  $\text{Conv}_4$  is a  $1 \times 1$  convolution for channel reduction. Combined with channel shuffle, this operation dynamically permutes channel subgroups to enhance inter-channel communication.

By fusing multi-scale context and enforcing channel diversity, the HFR amplifies suppressed high-frequency signals while filtering spatial redundancies. The refined features are then expanded back to channels and fused with residual branch outputs, providing enriched high-frequency information for subsequent components in HFEB.

2) *Depthwise Position-aware Attention (DPA)*: As shown in the Fig. 4 (b), given an input feature  $\mathbf{Y}_1 \in \mathbb{R}^{C \times H \times W}$ , a depthwise convolution (DWConv) is first applied to  $\mathbf{f}_{in}$ , expanding its channel dimension to  $3C \times H \times W$ . Following established multi-head attention frameworks, we perform channel-wise partitioning into  $h$  heads, each with  $\frac{C}{h}$  channels. This partitioning enables concurrent learning of distinct self-attention patterns across different feature subspaces. The partitioned feature map is then rearranged into  $Q$ ,  $K$  and  $V$  matrices of size, defined as:

$$Q, K, V = \text{RS}(\text{DWConv}_{3 \times 3}(\text{Conv}_5(\mathbf{Y}_1))), \quad (12)$$

where  $\text{Conv}_5$  is a  $1 \times 1$  convolution that expands channels from  $C$  to  $3C$ ,  $\text{DWConv}_{3 \times 3}$  denotes a  $3 \times 3$  depthwise convolution and  $\text{RS}$  denotes a reshape and split operator. To enhance positional modeling capabilities, we introduce a dynamical positional encoding mechanism. The input feature map is processed through a sub-network consisting of two  $1 \times 1 \times 1$  convolutions with GELU activation in between:

$$\mathbf{pos} = \text{Conv}_7 \cdot \text{GELU}(\text{Conv}_6 \cdot \mathbf{Y}_1), \quad (13)$$

where  $\text{Conv}_6, \text{Conv}_7$  denote  $1 \times 1$  convolutions. However, we observe that using positional encoding alone did not yield the desired performance. To further refine the attention mechanism, we introduce a temperature generator module using a series of linear transformations to generate a temperature scale

TABLE I: Ablation study of HFR on CelebA test [4].

Methods	Params	FLOPs	PSNR	SSIM
w/o HFR	–	–	28.16	0.8061
HFR w/o $CS$	0.353M	0.802G	28.20	0.8072
HFR w/ only $DWConv_{5 \times 5}$	0.316M	0.689G	28.15	0.8058
HFR w/ only $DWConv_{7 \times 7}$	0.390M	0.846G	28.18	<b>0.8077</b>
HFR	0.353M	0.802G	<b>28.21</b>	0.8075

**temp**, which **temp** can dynamically adjust attention scaling factors:

$$\mathbf{temp} = W_2 \cdot \text{GELU}(W_3 \cdot \mathbf{Y}_1), \quad (14)$$

where  $W_2, W_3$  denotes the linear layer, and **temp** represents the learnable temperature parameter. Unlike fixed-temperature scaling, this adaptive mechanism provides greater flexibility in capturing long-range dependencies. In summary, the attention scores are calculated by multiplying  $Q$  and  $K$ , and then scaled by the temperature value  $\alpha$ . The resulting attention-weighted  $V$  is combined with the original positional-aware features and finally reshaped back to the original feature map size. The complete attention computation can be formulated as:

$$\text{Attn}\{Q, K, V\} = V \cdot \text{RELU}(QK^T \cdot \mathbf{temp}) + \sigma(\mathbf{pos}), \quad (15)$$

where  $\sigma(\cdot)$  denotes a sigmoid activation.

#### D. Offsets mechanism

As shown in Fig. 2, instead of using residual connections between input and output as in existing methods [16], [23], [25] to boost original facial information, our approach employs an offset mechanism [45] to bridge the input with the residual features of multi-scale outputs. This design stems from the observation that fixed-grid sampling in traditional convolutional or upsampling operations often struggles to capture spatially variant misalignments, especially in areas with complex geometries or motion. To tackle this, our offset mechanism adaptively predicts and compensates for these misalignments by generating pixel-wise 2D displacement vectors through a lightweight convolutional predictor subnetwork, which analyzes the input features for precise feature alignment. Specifically, for the initial input  $\mathbf{f}_1$ :

$$\Delta \mathbf{r} = \mathbf{f}_{\text{offsets}}(\mathbf{f}_1) \in \mathbb{R}^{2 \times H \times W}, \mathbf{f}_3 = \phi(\mathbf{f}_2, \Delta \mathbf{r}), \quad (16)$$

where  $\Delta \mathbf{r}$  is the content-related offsets matrix,  $\phi(\cdot)$  denotes bilinear interpolation. Specifically, the offset-driven warping compensates for spatial misalignments caused by cascaded downsampling/upsampling operations, enhances high-frequency detail preservation through adaptively repositioning features according to local texture patterns, and promotes cross-scale feature consistency by aligning coarse-level structural information with fine-level details. Learned end-to-end without explicit supervision, this process allows the network to automatically find optimal spatial transformations that maximize feature coherence during reconstruction, which is especially crucial for keeping facial edge sharpness and structural integrity in FSR.

TABLE II: Ablation study of DPA on Helen test set [46]. The last line denotes the strategy used in our final model.

T_gen	T_para	P_emb	Params	FLOPs	PSNR	SSIM
	✓		–	–	26.99	0.8034
	✓	✓	0.162M	0.302G	26.97	0.8037
✓			0.325M	–	26.93	0.8008
✓		✓	0.325M	0.302G	<b>27.06</b>	<b>0.8064</b>

TABLE III: Ablation study of ASSB is conducted on the Helen test set [46] by replacing it with three representative alternatives: self-attention (SA) [47], convolutional blocks (Conv), and Vision State Space Block (VSSB) [31].

Methods	Params	FLOPs	PSNR	SSIM	VIF↑	LPIPS↓
SA	0.184M	0.113G	26.99	0.8035	0.4673	0.2231
CNN	0.287M	0.387G	27.01	0.8046	0.4691	0.2194
VSSB	0.269M	0.163G	27.02	0.8042	0.4697	0.2266
ASSB (Ours)	0.203M	0.125G	<b>27.06</b>	<b>0.8064</b>	<b>0.4706</b>	<b>0.2167</b>

## IV. EXPERIMENTS

### A. Datasets and Evaluation Metrics

We employ the CelebA [4] dataset for training and evaluate our model on three benchmarks: CelebA [4], Helen [46], and SCface [50]. Therefore, we crop the image based on its center point and resize it to  $128 \times 128$  pixels, serving as the high-resolution (HR) ground truth. Corresponding low-resolution (LR) inputs ( $16 \times 16$  pixels) are generated by downsampling HR images via bicubic interpolation. The training set comprises 18,000 images from CelebA, with 1,000 and 200 images reserved for testing and validation, respectively. For cross-dataset evaluation, we test on 50 samples from Helen and the SCface dataset without fine-tuning. We assess reconstruction quality using four widely adopted metrics: PSNR and SSIM [51] for pixel-level fidelity, LPIPS [52] for perceptual similarity, and VIF [53] for texture preservation.

### B. Implementation Details

Our FADPNet is implemented in PyTorch and trained on an *NVIDIA RTX 3090* GPU. We initialize the model with 32 channels and design its architecture across three distinct resolution levels. Specifically, the number of low-frequency modules is 2 at each level. Meanwhile, the number of HEFB modules is configured as follows: 2 in  $\mathbb{R}^{C \times H \times W}$  stage, 3 in  $\mathbb{R}^{2C \times \frac{H}{2} \times \frac{W}{2}}$  stage, and 4 in  $\mathbb{R}^{4C \times \frac{H}{4} \times \frac{W}{4}}$  stage. Optimization is performed using the Adam optimizer ( $\beta_1 = 0.9$  and  $\beta_2 = 0.99$ ) with an initial learning rate of  $2 \times 10^{-4}$ . The loss function combines reconstruction loss, and training converges within 150 epochs using a batch size of 16.

### C. Ablation Studies

1) *Effectiveness of HFR*: To further assess the impact of the HFR module in our model, we conduct an ablation study on the CelebA test set, as summarized in Table I. First, we evaluate the model without the HFR module. Removing HFR leads to a noticeable degradation in both PSNR and SSIM, indicating that the HFR module plays a crucial role in enhancing high-frequency details. We then investigate the influence of

TABLE IV: Quantitative comparisons for  $\times 8$  SR on the CelebA and Helen test sets.

Methods	Params $\downarrow$	Speed $\downarrow$	CelebA [4]				Helen [46]			
			PSNR $\uparrow$	SSIM $\uparrow$	VIF $\uparrow$	LPIPS $\downarrow$	PSNR $\uparrow$	SSIM $\uparrow$	VIF $\uparrow$	LPIPS $\downarrow$
Bicubic	–	–	23.61	0.6779	0.1821	0.4899	22.95	0.6762	0.1745	0.4912
FSRNet [13]	27.5M	89.8ms	27.05	0.7714	0.3852	0.2127	25.45	0.7364	0.3482	0.3090
DIC [14]	22.8M	120.5ms	27.42	0.7840	0.4234	0.2129	26.15	0.7717	0.4085	<b>0.2158</b>
SPARNet [16]	10.6M	36.6ms	27.73	0.7949	0.4505	0.1995	26.43	0.7839	0.4262	0.2674
SISN [18]	9.8M	68ms	27.91	0.7971	0.4785	0.2005	26.64	0.7908	0.4623	0.2571
AD-GNN [19]	15.8M	107.9ms	27.82	0.7962	0.4470	0.1937	26.57	0.7786	0.4363	0.2423
Restormer-M [47]	11.7M	63.2ms	27.94	0.8027	0.4624	0.1933	<u>26.91</u>	<u>0.8013</u>	0.4595	0.2432
LAAT [20]	22.4M	<u>35.3ms</u>	27.91	0.7794	0.4624	0.1879	26.89	0.8005	0.4569	0.2255
ELSFace [48]	<u>8.7M</u>	<b>24ms</b>	27.96	0.7992	0.4783	0.1927	26.70	0.7910	0.4442	0.2495
SFMNet [22]	<b>8.6M</b>	49.2ms	27.96	0.7996	0.4644	0.1937	26.86	0.7987	0.4573	0.2322
SPADNet [49]	13.2M	52ms	27.82	0.7966	0.4589	0.1987	26.41	0.7857	0.4295	0.2645
FreqFormer [36]	9.9M	75ms	<u>28.15</u>	<u>0.8047</u>	<b>0.4883</b>	<u>0.1851</u>	26.82	0.7973	<u>0.4678</u>	0.2290
<b>FADPNet (Ours)</b>	<b>8.6M</b>	39.6ms	<b>28.21</b>	<b>0.8075</b>	<u>0.4876</u>	<b>0.1741</b>	<b>27.06</b>	<b>0.8064</b>	<b>0.4706</b>	<u>0.2167</u>

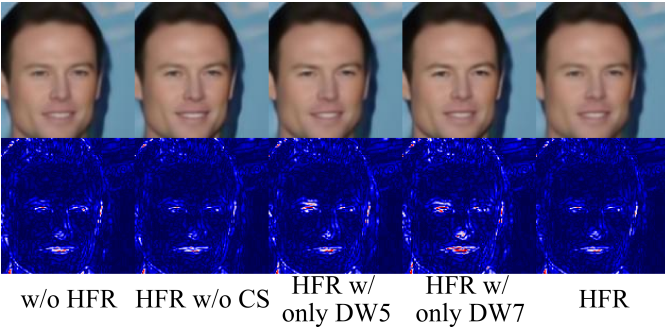


Fig. 5: Comparisons of error maps on our HFR. Redder regions indicate larger pixel-wise errors. The complete HFR module in our FADPNet leads to the lowest residual errors and shows superior ability to restore high-frequency facial details.

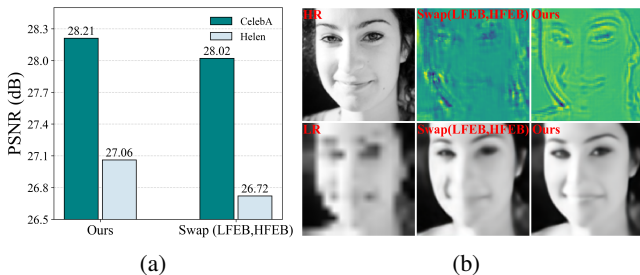


Fig. 6: (a) Ablation studies of the effectiveness of frequency-specific modules on the CelebA [4] and Helen datasets [46]. “swap” is our model in which the low- and high-frequency blocks are swapped, resulting in a noticeable performance drop compared to our original model. (b) Feature map visualization and FSR results between our original model and swapped-frequency variant show our modules design for different frequency features produces sharp and accurate facial contours.

different depth-wise convolution kernel configurations. When using only the  $5 \times 5$  kernel, the model achieves a PSNR of 28.15 and SSIM of 0.8058, slightly below the performance of the configuration that employs both kernels. This suggests that the  $5 \times 5$  kernel is effective at capturing localized details but insufficient for modeling a wide range of high-frequency information. In contrast, using only the  $7 \times 7$  kernel yields a PSNR of 28.18 and SSIM of 0.8077, indicating its superiority

TABLE V: Ablation study of our attention strategy on CelebA [4] and Helen [46] test set.

Methods	CelebA		Helen	
	PSNR / SSIM	PSNR / SSIM	PSNR / SSIM	PSNR / SSIM
LFEB w/o SEB	28.16 / 0.8067	26.99 / 0.8043		
HFEB w/o DPA	28.04 / 0.8032	26.80 / 0.7981		
w/o offsets	28.17 / 0.8073	27.00 / 0.8050		
Ours	<b>28.21 / 0.8075</b>	<b>27.06 / 0.8064</b>		

in capturing broader contextual features. However, it still underperforms compared to the full HFR setup. Adding an extra  $3 \times 3$  kernel results in a marginal performance drop (PSNR: 28.16, SSIM: 0.8070), implying that this addition does not significantly enhance detail restoration. Moreover, removing the channel shuffle (CS) operation causes a slight decrease in both PSNR and SSIM, highlighting the importance of inter-channel interaction in feature representation. To further validate these observations, we present residual heatmaps visualizing the pixel-wise differences between the reconstructed outputs and their HR counterparts.

As shown in Fig. 5, the model without the HFR module exhibits prominent errors, especially in regions rich in high-frequency textures such as facial contours. The model with HFR but without CS shows moderate improvement, suggesting that the main structure of HFR still contributes positively even without CS. Models employing only a single kind of depth-wise convolution kernel exhibit complementary characteristics: the  $5 \times 5$  kernel better preserves localized features while missing global structures, whereas the  $7 \times 7$  kernel captures larger-scale patterns but struggles with fine textures. In contrast, the full HFR achieves the lowest errors, visually affirming its superior capacity for high-frequency detail restoration and consistent with its leading PSNR and SSIM scores.

2) *Effectiveness of DPA*: To comprehensively evaluate the individual and synergistic effects of components in our proposed Depthwise Position-aware Attention (DPA) module, we perform systematic ablation studies on the Helen test set [1], with detailed results presented in Table II. Our investigation focuses on three critical elements: the learnable temperature generator (T\_gen), fixed temperature parameter (T\_para), and positional embedding (P\_emb), analyzing their impacts on both reconstruction quality and model complexity.

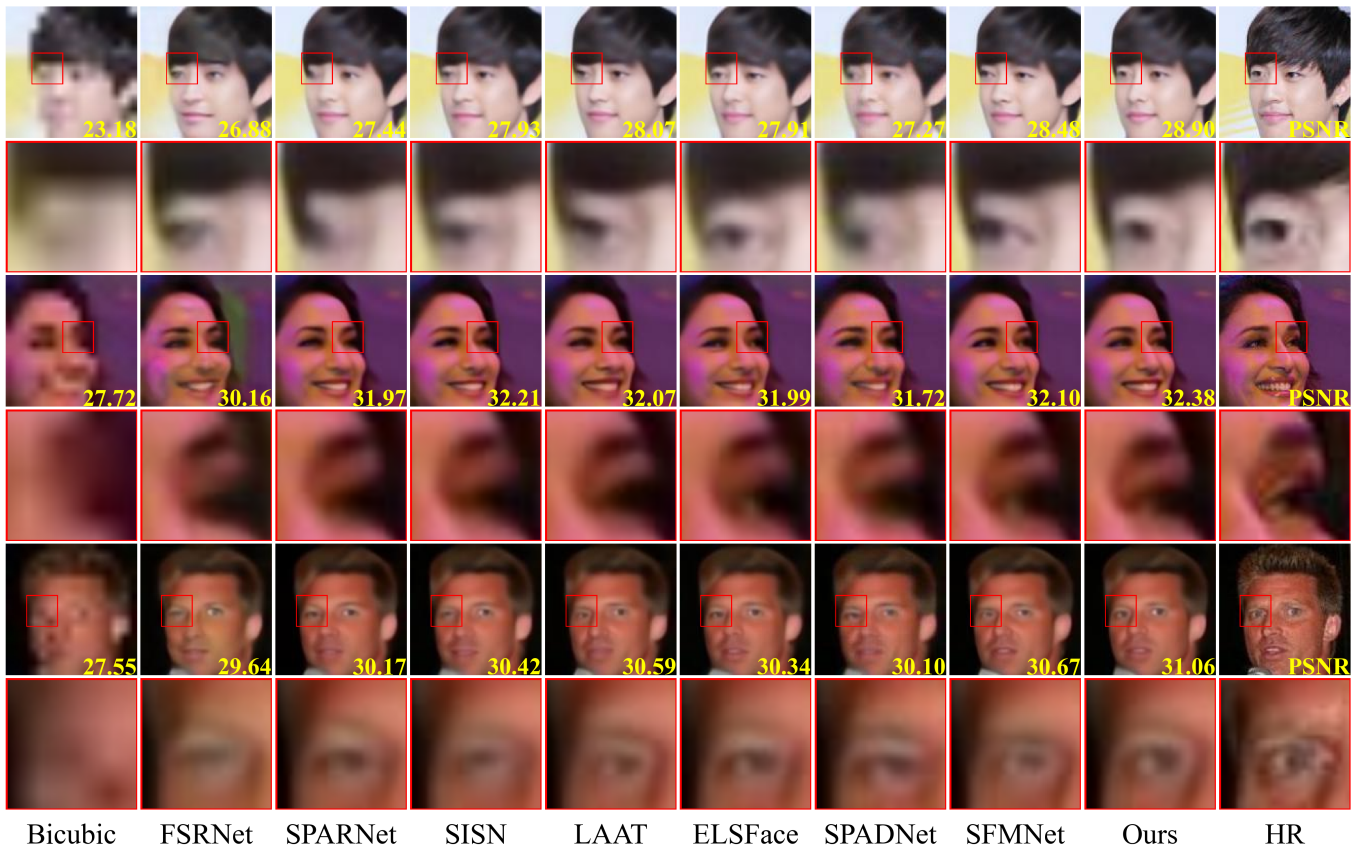


Fig. 7: Visual comparisons for  $\times 8$  SR on the CelebA test set [4]. Our FADPNet can reconstruct clear face images.

The initial configuration with only  $T_{para}$  provides a baseline level of reconstruction, but its fixed scaling restricts adaptability to spatial and contextual variations, resulting in suboptimal attention modulation for detailed facial regions. Adding  $P_{emb}$  to  $T_{para}$  slightly improves SSIM, suggesting better structural preservation, though PSNR shows a marginal decline. The  $P_{emb}$  component enables more precise localization of structural details, particularly in semantically critical facial regions like ocular areas, nasal contours, and lip boundaries. Our FADPNet combines  $T_{gen}$  with  $P_{emb}$ , achieving peak performance. This configuration establishes a synergistic relationship where  $T_{gen}$  dynamically modulates attention sharpness according to local content complexity, while  $P_{emb}$  ensures spatial consistency in feature aggregation. Notably, implementing  $T_{gen}$  without  $P_{emb}$  guidance degrades performance. This reveals that without spatial constraints, the self-learned scaling factors may produce inconsistent attention distributions, particularly in homogeneous facial regions where positional cues are crucial for accurate feature matching.

These systematic experiments validate the necessity of integrating both adaptive temperature scaling and explicit spatial encoding in our DPA design. The final architecture achieves superior performance through three key mechanisms: (a) Content-aware attention sharpness adaptation via  $T_{gen}$ , (b) Geometry-preserving feature aggregation through  $P_{emb}$ , and (c) Computational efficiency from depthwise implementation. The results demonstrate our module’s effectiveness in

addressing the unique challenges of facial super-resolution, particularly in preserving identity-critical details while maintaining natural texture synthesis.

3) *Effectiveness of ASSB*: To evaluate the suitability of the Attentive State Space Block (ASSB) for low-frequency modeling in our method, we conduct ablation studies by replacing it with three representative alternatives: self-attention (SA) [47], residual block (CNN) [54], and Vision State Space Block (VSSB) [31]. As shown in Table III, our full model with ASSB achieves the best overall performance, indicating superior perceptual quality and structural fidelity.

It is worth noting that ASSB is not our original design, but a recently proposed state-space module tailored for long-range dependency modeling. In our framework, we integrate ASSB within LFEB to exploit its strength in global structure preservation. Unlike Conv, which tends to focus on local or high-frequency features, ASSB’s non-causal state-space formulation excels at capturing smooth, spatially consistent facial regions such as contours and skin tones. Its built-in low-rank prompt decomposition also aids in suppressing high-frequency noise and promotes stable propagation across homogeneous areas. Compared to the more general-purpose VSSB, ASSB offers a lighter structure and better frequency selectivity when dealing with low-frequency signals. Despite using fewer parameters (0.203M vs. 0.269M), ASSB outperforms or matches VSSB in all metrics, demonstrating its superior efficiency-to-performance ratio when applied to

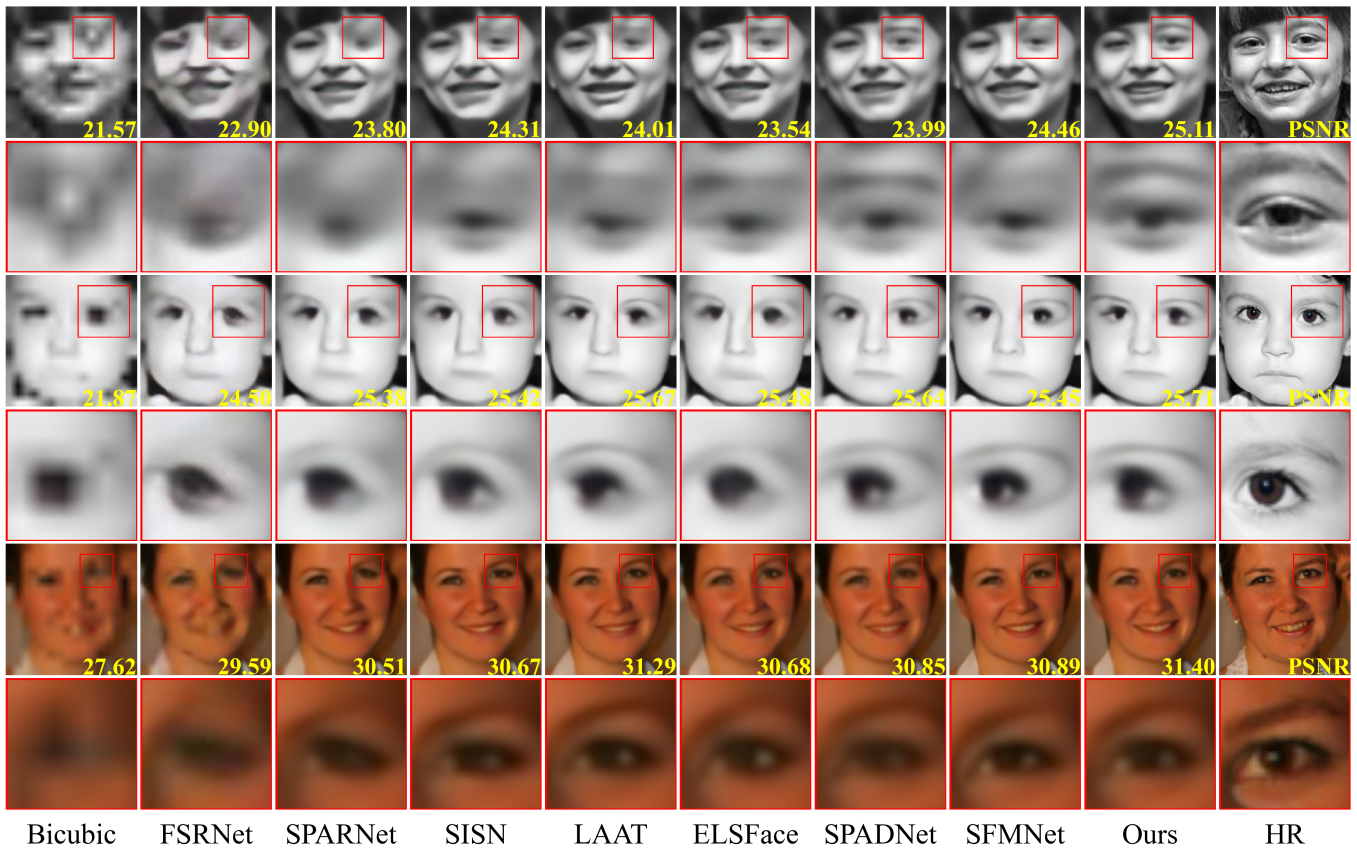


Fig. 8: Visual comparisons for  $\times 8$  SR on the Helen test set [46]. Our FADPNet can reconstruct clear face images.

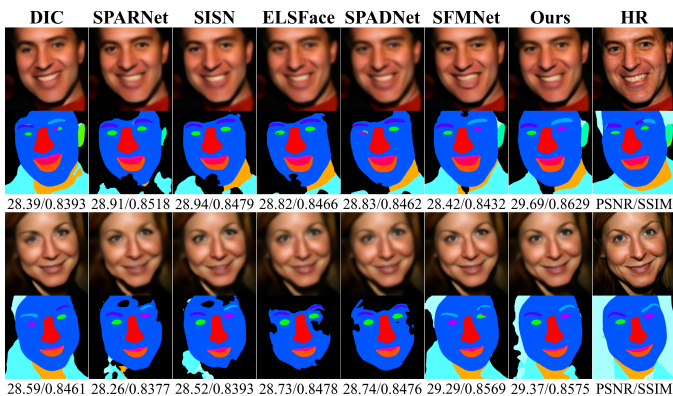


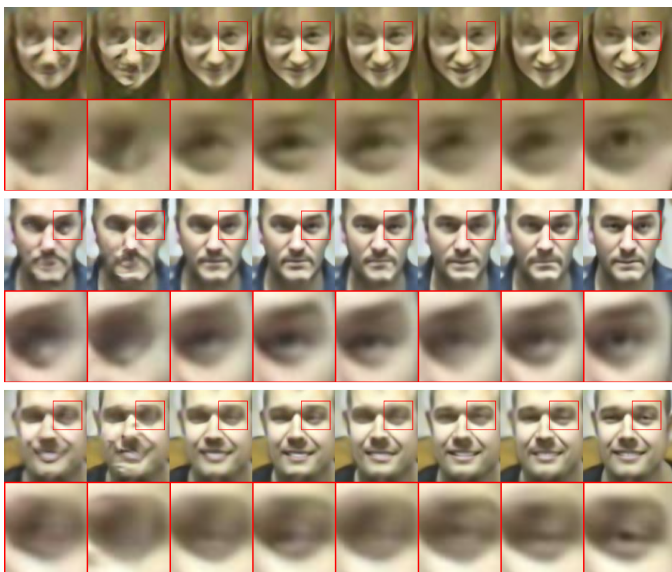
Fig. 9: Visual comparisons with existing methods on downstream tasks, like face parsing.

low-frequency pathways. These results collectively justify our choice of ASSB as the most effective backbone for global low-frequency modeling in our frequency-aware architecture. Its integration helps maintain large-scale facial coherence and mitigates structural misalignment—challenges that conventional transformer or Conv-based designs struggle to address.

4) *Study of the architecture of low- and high-frequency modules:* To investigate the effectiveness of low- and high-frequency architecture, we conduct an ablation study on the CelebA and Helen datasets by interchanging the positions of the low-frequency enhancement block (LFEB) and

high-frequency enhancement block (HFEB). As illustrated in Fig. 6a, this modification leads to a consistent drop in PSNR across both datasets, highlighting the critical importance of the original frequency-aware design. The original model achieves superior reconstruction performance by appropriately allocating low- and high-frequency processing to their respective branches. In contrast, the swapped configuration disrupts this balance, resulting in suboptimal representation and degraded image quality. Fig. 6b visually compares the original and the swapped variants. The results clearly show that the proposed model preserves facial structures and fine details more effectively, yielding sharper contours and more realistic textures. Conversely, the swapped version produces noticeably blurrier outputs, especially around facial components like eyes and mouth, further validating the necessity of maintaining the original design of frequency-specific modules.

5) *Study of local-global attention strategy:* As summarized in Table V, our goal is to examine the individual contributions of local and global modeling components in both high- and low-frequency enhancement branches. First, we remove the squeeze-and-excitation block from LFEB. The performance drops on CelebA and Helen. This suggests that incorporating squeeze-and-excitation operations to extract low-frequency global interactions and emphasize informative channels is beneficial, even in smooth regions. These global interactions help preserve structurally important facial components that might otherwise be weakened in low-frequency representa-



FSRNet FACN SPARNet SISR ADGNN LAAT SFMNet Ours

Fig. 10: Visual comparison on SCface [50] of real surveillance scenarios for  $\times 8$  SR. Our FADPNet can reconstruct clear face components.

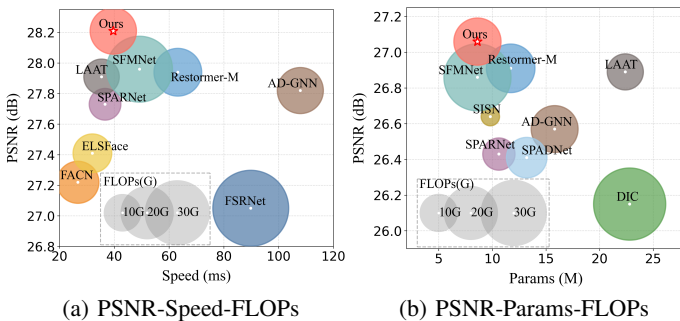


Fig. 11: (a) PSNR, FLOPs, and speed tradeoffs on the CelebA test set [4]. (b) PSNR, FLOPs, and Params tradeoffs on the Helen test set [46], showing the balance of our method.

tions. Next, we remove the DPA module from HFEB. The result shows a more noticeable degradation, with performance dropping to 28.04 / 0.8032 on CelebA and 26.80 / 0.7981 on Helen. This highlights the crucial role of DPA in capturing localized textures and reducing artifacts in high-frequency content. Finally, removing the offset mechanism causes a moderate decline in performance, indicating that it contributes to cross-scale feature alignment.

#### D. Comparison with Other Methods

In this section, we conduct a comprehensive comparison of our proposed method against state-of-the-art (SOTA) techniques in FSR, encompassing general image SR methods like RCAN [54], Restormer-M [47] and FreqFormer [36], specialized FSR approaches such as FSRNet [13], DIC [14], SPARNet [16], AD-GNN [19], SISR [18], LAAT [20], SFMNet [22], ELSFace [48], and SPADNet [49]. All methods are trained on the CelebA [4] dataset under identical settings—including preprocessing, loss functions, and optimizer

TABLE VI: Quantitative comparison on face average similarity with existing methods on SCface [50] of real surveillance scenarios.

Methods	Average Similarity				
	Case 1	Case 2	Case 3	Case 4	Case 5
RCAN [54]	0.5481	0.5776	0.4441	0.7139	0.5754
FSRNet [13]	0.4930	0.5212	0.5487	0.6544	0.5276
FACN [55]	0.3670	0.3309	0.3326	0.5612	0.4373
SPARNet [16]	0.6382	0.6412	0.6455	0.6670	0.6259
SISR [18]	0.6182	0.6471	0.6354	0.7011	0.6469
AD-GNN [19]	0.6151	0.6664	0.6432	0.7213	0.6034
LAAT [20]	0.6083	0.7394	0.7282	0.7157	0.5965
SFMNet [22]	0.6240	0.6048	0.6330	0.7158	0.5742
<b>Ours</b>	<b>0.6782</b>	<b>0.7412</b>	<b>0.7592</b>	<b>0.7714</b>	<b>0.6623</b>

configurations—to eliminate implementation biases and ensure direct attribution of performance differences to architectural innovations.

1) *Comparison on the CelebA dataset and the Helen dataset:* We present the quantitative results for the CelebA and Helen test datasets in Table IV. The best and second-best results are highlighted in bold and underlined, respectively. These results demonstrate the strength of our architecture in balancing structural accuracy and perceptual quality. To further evaluate the generalization ability of our method, we directly apply the model trained on CelebA to the Helen test set. The quantitative results for  $\times 8$  FSR are also presented in Table IV, showing that our method comprehensively outperforms other approaches. Despite having only 8.6M parameters (similar to SFMNet [22]), our FADPNet achieves 39.6ms inference speed, which is 1.8 $\times$  faster than FreqFormer [36] (75ms) and comparable to lightweight methods like SPARNet [16] (36.6ms). Compared to ELSFace [48], despite the similar parameter counts (8.6M vs. 8.7M), FADPNet improves PSNR by 0.25dB on CelebA and 0.36dB on Helen. As summarized in Fig. 7 and Fig. 8, while competing methods often produce blurred facial contours and distorted features (e.g., ill-defined eyes), our reconstructions successfully preserve sharp edges, facial symmetry, and fine-grained details (e.g., eyeball), closely aligning with the ground-truth HR images. As shown in Fig. 9, we also use the face parsing model [56] to analyze the FSR results of different models on the Helen dataset. The visual results clearly demonstrate that our method produces the most complete and accurate facial structure, preserving better face details than competing models. In summary, while existing methods struggle with blurred shapes and significant detail loss, our model effectively preserves facial contours and fine details. This highlights not only the robustness of our approach across different datasets but also its superiority over SOTA techniques in both performance and efficiency.

#### 2) Comparison on real-world surveillance scenarios:

Restoring facial details from real-world surveillance imagery remains a formidable challenge due to inherent low resolution, uncontrolled lighting, and sensor noise—factors that are often inadequately captured in synthetic benchmarks. To address this, we conduct experiments using low-quality face images from the SCface dataset [50], which inherently represents real-

world surveillance scenarios without manual downsampling. As illustrated in Fig. 10, visual comparisons reveal that existing methods often struggle to reconstruct critical facial features due to the challenges posed by noisy, low-resolution inputs, leading to blurred contours and loss of texture details. In contrast, our FADPNet leverages adaptive feature separation and dual frequency enhancement, effectively restoring sharper facial structures, finer textures, and more natural facial symmetry. Beyond visual fidelity, we assess the impact on downstream tasks such as face matching, comparing the similarity between restored faces and their corresponding high-definition reference images. Table VI presents the quantitative results, demonstrating that our approach consistently achieves higher similarity scores across multiple test cases. This confirms its practical applicability in challenging surveillance scenarios.

3) *Model Complexity Analysis*: Beyond reconstruction quality, we conduct a comprehensive evaluation of model efficiency in terms of parameter count and inference speed, both of which are crucial for devices with limited computing resources. At each stage, inputs are dynamically decomposed into high-frequency and low-frequency components, which are then processed by our specialized sub-networks: a CNN branch tailored for capturing high-frequency facial details, and a Mamba-based branch better suited for modeling low-frequency, long-range dependencies. This innovative design achieves an optimal balance between computational efficiency and an enhanced representational capacity for high-frequency details. By leveraging this structured decomposition, our model adeptly handles complex facial features, leading to improved performance in FSR. As shown in Fig. 11a and Fig. 11b, our method demonstrates an excellent trade-off between reconstruction accuracy and computational cost. Specifically, Fig. 11a illustrates that our approach surpasses existing methods over 0.2dB PSNR with lower FLOPs and faster inference speed on the CelebA test set, highlighting its practical efficiency. Similarly, Fig. 11b further shows that on the Helen test set, our method maintains superior PSNR while keeping the parameter count relatively low, outperforming most existing methods in both accuracy and model compactness. Overall, our approach achieves a well-balanced trade-off between model size, inference speed, and reconstruction quality, making it effective.

## V. LIMITATIONS AND FUTURE WORKS

Despite the dual-path design that independently captures low- and high-frequency information, the current fusion strategy is relatively simplistic and may fail to fully exploit the complementary nature of these frequency components, resulting in suboptimal recovery of fine-grained facial details. Moreover, the model demonstrates a performance bias toward frontal faces, showing reduced robustness when handling side views or large pose variations, due to limited diversity in training views. In future work, we plan to investigate more effective fusion mechanisms between the high- and low-frequency branches to enhance inter-frequency interaction and detail restoration. Additionally, we will consider incorporating pose-aware augmentation or multi-view training strategies to

improve generalization to non-frontal faces, further improving the model’s robustness in practical applications.

## VI. CONCLUSIONS

In this paper, we propose FADPNet, a frequency-aware dual-path network that separates and processes low- and high-frequency components for the frequency imbalance problem in face super-resolution. The Low-Frequency Enhancement Block (LFEB), comprising ASSB and SEB, models global context and reinforces identity-consistent features. In parallel, the High-Frequency Enhancement Block (HFEB), built with DPA and HFR, refines local structures through adaptive attention mechanisms. This frequency-specific design enables more effective resource allocation and promotes both structural coherence and fine-detail recovery. Extensive experiments validate the superiority of our method in the reconstruction of face image quality and computational efficiency, underscoring the effectiveness of our proposed strategy.

## REFERENCES

- [1] F. Schroff, D. Kalenichenko, and J. Philbin, “Facenet: A unified embedding for face recognition and clustering,” in *Proceedings of the IEEE Conference on Computer Vision and Pattern Recognition (CVPR)*, 2015, pp. 815–823.
- [2] X. Zhu, Z. Lei, X. Liu, H. Shi, and S. Z. Li, “Face alignment across large poses: A 3d solution,” in *Proceedings of the IEEE Conference on Computer Vision and Pattern Recognition (CVPR)*, 2016, pp. 146–155.
- [3] S. I. Serengil and A. Ozpinar, “Hyperextended lightface: A facial attribute analysis framework,” in *Proceedings of the International Conference on Engineering and Emerging Technologies (ICEET)*. IEEE, 2021, pp. 1–4.
- [4] Z. Liu, P. Luo, X. Wang, and X. Tang, “Deep learning face attributes in the wild,” in *Proceedings of the IEEE International Conference on Computer Vision (ICCV)*, 2015, pp. 3730–3738.
- [5] Y. Tian, H. Chen, C. Xu, and Y. Wang, “Image processing gnn: Breaking rigidity in super-resolution,” in *Proceedings of the IEEE/CVF Conference on Computer Vision and Pattern Recognition (CVPR)*, 2024, pp. 24 108–24 117.
- [6] Y. Gou, P. Hu, J. Lv, H. Zhu, and X. Peng, “Rethinking image super resolution from long-tailed distribution learning perspective,” in *Proceedings of the IEEE/CVF Conference on Computer Vision and Pattern Recognition (CVPR)*, 2023, pp. 14 327–14 336.
- [7] W. Xie, D. Song, C. Xu, C. Xu, H. Zhang, and Y. Wang, “Learning frequency-aware dynamic network for efficient super-resolution,” in *Proceedings of the IEEE/CVF International Conference on Computer Vision (ICCV)*, 2021, pp. 4308–4317.
- [8] D. Kim, M. Kim, G. Kwon, and D.-S. Kim, “Progressive face super-resolution via attention to facial landmark,” in *Proceedings of the 30th British Machine Vision Conference (BMVC)*, 2019.
- [9] N. Ketkar, J. Moolayil, N. Ketkar, and J. Moolayil, “Convolutional neural networks,” *Deep learning with Python: learn best practices of deep learning models with PyTorch*, pp. 197–242, 2021.
- [10] A. Gu and T. Dao, “Mamba: Linear-time sequence modeling with selective state spaces,” *arXiv preprint arXiv:2312.00752*, 2023.
- [11] A. Vaswani, N. Shazeer, N. Parmar, J. Uszkoreit, L. Jones, A. N. Gomez, E. Kaiser, and I. Polosukhin, “Attention is all you need,” in *Proceedings of the Advances in Neural Information Processing Systems (NeurIPS)*, 2017, pp. 5998–6008.
- [12] W. Li, M. Wang, K. Zhang, J. Li, X. Li, Y. Zhang, G. Gao, W. Deng, and C.-W. Lin, “Survey on deep face restoration: From non-blind to blind and beyond,” *arXiv:2309.15490*, 2023.
- [13] Y. Chen, Y. Tai, X. Liu, C. Shen, and J. Yang, “Fsrnet: End-to-end learning face super-resolution with facial priors,” in *Proceedings of the IEEE Conference on Computer Vision and Pattern Recognition (CVPR)*, 2018, pp. 2492–2501.
- [14] C. Ma, Z. Jiang, Y. Rao, J. Lu, and J. Zhou, “Deep face super-resolution with iterative collaboration between attentive recovery and landmark estimation,” in *Proceedings of the IEEE Conference on Computer Vision and Pattern Recognition (CVPR)*, 2020, pp. 5569–5578.

- [15] X. Hu, W. Ren, J. LaMaster, X. Cao, X. Li, Z. Li, B. Menze, and W. Liu, "Face super-resolution guided by 3d facial priors," in *Proceedings of the European Conference on Computer Vision (ECCV)*, 2020, pp. 763–780.
- [16] C. Chen, D. Gong, H. Wang, Z. Li, and K.-Y. K. Wong, "Learning spatial attention for face super-resolution," *IEEE Transactions on Image Processing*, vol. 30, pp. 1219–1231, 2021.
- [17] L. Peng, W. Li, R. Pei, J. Ren, J. Xu, Y. Wang, Y. Cao, and Z.-J. Zha, "Towards realistic data generation for real-world super-resolution," in *Proceedings of the International Conference on Learning Representations (ICLR)*, 2025.
- [18] T. Lu, Y. Wang, Y. Zhang, Y. Wang, L. Wei, Z. Wang, and J. Jiang, "Face hallucination via split-attention in split-attention network," in *Proceedings of the ACM International Conference on Multimedia (ACM MM)*, 2021, pp. 5501–5509.
- [19] Q. Bao, B. Gang, W. Yang, J. Zhou, and Q. Liao, "Attention-driven graph neural network for deep face super-resolution," *IEEE Transactions on Image Processing*, vol. 31, pp. 6455–6470, 2022.
- [20] G. Li, J. Shi, Y. Zong, F. Wang, T. Wang, and Y. Gong, "Learning attention from attention: Efficient self-refinement transformer for face super-resolution." in *Proceedings of the International Joint Conference on Artificial Intelligence (IJCAI)*, 2023, pp. 1035–1043.
- [21] Q. Bao, Y. Liu, B. Gang, W. Yang, and Q. Liao, "Sctanet: A spatial attention-guided cnn-transformer aggregation network for deep face image super-resolution," *IEEE Transactions on Multimedia*, vol. 25, pp. 8554–8565, 2023.
- [22] C. Wang, J. Jiang, Z. Zhong, and X. Liu, "Spatial-frequency mutual learning for face super-resolution," in *Proceedings of the IEEE/CVF Conference on Computer Vision and Pattern Recognition (CVPR)*, 2023, pp. 22 356–22 366.
- [23] W. Li, H. Guo, X. Liu, K. Liang, J. Hu, Z. Ma, and J. Guo, "Efficient face super-resolution via wavelet-based feature enhancement network," in *Proceedings of the ACM International Conference on Multimedia (ACM MM)*, 2024, pp. 4515–4523.
- [24] W. Li, J. Li, G. Gao, W. Deng, J. Yang, G.-J. Qi, and C.-W. Lin, "Efficient image super-resolution with feature interaction weighted hybrid network," *IEEE Transactions on Multimedia*, vol. 27, pp. 2256–2267, 2025.
- [25] G. Gao, Z. Xu, J. Li, J. Yang, T. Zeng, and G.-J. Qi, "Ctcnet: A cnn-transformer cooperation network for face image super-resolution," *IEEE Transactions on Image Processing*, vol. 32, pp. 1978–1991, 2023.
- [26] J. Liang, J. Cao, G. Sun, K. Zhang, L. Van Gool, and R. Timofte, "Swinir: Image restoration using swin transformer," in *Proceedings of the IEEE/CVF International Conference on Computer Vision (ICCV)*, 2021, pp. 1833–1844.
- [27] W. Li, J. Li, G. Gao, W. Deng, J. Zhou, J. Yang, and G.-J. Qi, "Cross-receptive focused inference network for lightweight image super-resolution," *IEEE Transactions on Multimedia*, vol. 26, pp. 864–877, 2023.
- [28] A. Gu, K. Goel, and C. Ré, "Efficiently modeling long sequences with structured state spaces," *arXiv preprint arXiv:2111.00396*, 2021.
- [29] J. Ma, F. Li, and B. Wang, "U-mamba: Enhancing long-range dependency for biomedical image segmentation," *arXiv preprint arXiv:2401.04722*, 2024.
- [30] L. Peng, X. Di, Z. Feng, W. Li, R. Pei, Y. Wang, X. Fu, Y. Cao, and Z.-J. Zha, "Directing mamba to complex textures: An efficient texture-aware state space model for image restoration," in *Proceedings of the International Joint Conference on Artificial Intelligence (IJCAI)*, 2025.
- [31] H. Guo, J. Li, T. Dai, Z. Ouyang, X. Ren, and S.-T. Xia, "Mambair: A simple baseline for image restoration with state-space model," in *Proceedings of the European Conference on Computer Vision (ECCV)*. Springer, 2024, pp. 222–241.
- [32] J. Weng, Z. Yan, Y. Tai, J. Qian, J. Yang, and J. Li, "Mamballie: Implicit retinex-aware low light enhancement with global-then-local state space," *arXiv preprint arXiv:2405.16105*, 2024.
- [33] H. Guo, Y. Guo, Y. Zha, Y. Zhang, W. Li, T. Dai, S.-T. Xia, and Y. Li, "Mambairv2: Attentive state space restoration," in *Proceedings of the IEEE/CVF Conference on Computer Vision and Pattern Recognition (CVPR)*, 2025.
- [34] S. Li, Q. Cai, H. Li, J. Cao, L. Wang, and Z. Li, "Frequency separation network for image super-resolution," *IEEE Access*, vol. 8, pp. 33 768–33 777, 2020.
- [35] R. Cai, Y. Ding, and H. Lu, "Freqnet: A frequency-domain image super-resolution network with discrete cosine transform," *arXiv preprint arXiv:2111.10800*, 2021.
- [36] T. Dai, J. Wang, H. Guo, J. Li, J. Wang, and Z. Zhu, "Freqformer: frequency-aware transformer for lightweight image super-resolution," in *Proceedings of the International Joint Conference on Artificial Intelligence (IJCAI)*, 2024, pp. 731–739.
- [37] W. Li, H. Guo, Y. Hou, G. Gao, and Z. Ma, "Dual-domain modulation network for lightweight image super-resolution," *arXiv preprint arXiv:2503.10047*, 2025.
- [38] Z. Zhong, T. Shen, Y. Yang, Z. Lin, and C. Zhang, "Joint sub-bands learning with clique structures for wavelet domain super-resolution," *Proceedings of the Advances in Neural Information Processing Systems (NeurIPS)*, vol. 31, 2018.
- [39] F. Zhou, X. Li, and Z. Li, "High-frequency details enhancing densenet for super-resolution," *Neurocomputing*, vol. 290, pp. 34–42, 2018.
- [40] L. Peng, Y. Cao, Y. Sun, and Y. Wang, "Lightweight adaptive feature de-drifting for compressed image classification," *IEEE Transactions on Multimedia*, vol. 26, pp. 6424–6436, 2024.
- [41] D. Qu, L. Li, and R. Yao, "Frequency-separated attention network for image super-resolution," *Applied Sciences*, vol. 14, no. 10, p. 4238, 2024.
- [42] O. Ronneberger, P. Fischer, and T. Brox, "U-net: Convolutional networks for biomedical image segmentation," in *Proceedings of the International Conference on Medical Image Computing and Computer-Assisted Intervention (MICCAI)*. Springer, 2015, pp. 234–241.
- [43] J. Hu, L. Shen, and G. Sun, "Squeeze-and-excitation networks," in *Proceedings of the IEEE Conference on Computer Vision and Pattern Recognition (CVPR)*, 2018, pp. 7132–7141.
- [44] E. Jang, S. Gu, and B. Poole, "Categorical reparameterization with gumbel-softmax," *arXiv preprint arXiv:1611.01144*, 2016.
- [45] Y. Wang, Y. Liu, S. Zhao, J. Li, and L. Zhang, "Camixers: Only details need more" attention," in *Proceedings of the IEEE/CVF Conference on Computer Vision and Pattern Recognition (CVPR)*, 2024, pp. 25 837–25 846.
- [46] V. Le, J. Brandt, Z. Lin, L. Bourdev, and T. S. Huang, "Interactive facial feature localization," in *Proceedings of the European Conference on Computer Vision (ECCV)*, 2012, pp. 679–692.
- [47] S. W. Zamir, A. Arora, S. Khan, M. Hayat, F. S. Khan, and M.-H. Yang, "Restormer: Efficient transformer for high-resolution image restoration," in *Proceedings of the IEEE/CVF Conference on Computer Vision and Pattern Recognition (CVPR)*, 2022, pp. 5728–5739.
- [48] H. Qi, Y. Qiu, X. Luo, and Z. Jin, "An efficient latent style guided transformer-cnn framework for face super-resolution," *IEEE Transactions on Multimedia*, vol. 26, pp. 1589–1599, 2024.
- [49] C. Wang, J. Jiang, K. Jiang, and X. Liu, "Structure prior-aware dynamic network for face super-resolution," *IEEE Transactions on Biometrics, Behavior, and Identity Science*, vol. 6, no. 3, pp. 326–340, 2024.
- [50] M. Grgic, K. Delac, and S. Grgic, "Sface—surveillance cameras face database," *Multimedia Tools and Applications*, vol. 51, no. 3, pp. 863–879, 2011.
- [51] Z. Wang, A. C. Bovik, H. R. Sheikh, and E. P. Simoncelli, "Image quality assessment: from error visibility to structural similarity," *IEEE Transactions on Image Processing*, vol. 13, no. 4, pp. 600–612, 2004.
- [52] R. Zhang, P. Isola, A. A. Efros, E. Shechtman, and O. Wang, "The unreasonable effectiveness of deep features as a perceptual metric," in *Proceedings of the IEEE Conference on Computer Vision and Pattern Recognition (CVPR)*, 2018, pp. 586–595.
- [53] H. R. Sheikh and A. C. Bovik, "Image information and visual quality," *IEEE Transactions on Image Processing*, vol. 15, no. 2, pp. 430–444, 2006.
- [54] Y. Zhang, K. Li, K. Li, L. Wang, B. Zhong, and Y. Fu, "Image super-resolution using very deep residual channel attention networks," in *Proceedings of the European Conference on Computer Vision (ECCV)*, 2018, pp. 286–301.
- [55] J. Xin, N. Wang, X. Jiang, J. Li, X. Gao, and Z. Li, "Facial attribute capsules for noise face super resolution," in *Proceedings of the AAAI Conference on Artificial Intelligence (AAAI)*, 2020, pp. 12 476–12 483.
- [56] C. Yu, J. Wang, C. Peng, C. Gao, G. Yu, and N. Sang, "Bisenet: Bilateral segmentation network for real-time semantic segmentation," in *Proceedings of the European conference on computer vision (ECCV)*, 2018, pp. 325–341.